Chinese Journal of Natural Medicines

Targeting senescence-associated fibrotic signatures identifies syringin as an effective modulator of the ATR/CHK1p53 axis in idiopathic pulmonary fibrosis

Yuyang Wang, Guanghui Yin, Mixing Niu, Wei Wang, Zhenyun Liao, Lei Yang, Chunli Wu, Yu Cao, Kai Gao, Zhaoxing Dong

Citation: Yuyang Wang, Guanghui Yin, Mixing Niu, Wei Wang, Zhenyun Liao, Lei Yang, Chunli Wu, Yu Cao, Kai Gao, Zhaoxing Dong, Targeting senescence-associated fibrotic signatures identifies syringin as an effective modulator of the ATR/CHK1p53 axis in idiopathic pulmonary fibrosis, Chinese Journal of Natural Medicines, 2026, 24(10), 1205-1220. doi: 10.1016/S1875-5364(26)61215-0.

View online: https://doi.org/10.1016/S1875-5364(26)61215-0

Related articles that may interest you

Neotuberostemonine and tuberostemonine ameliorate pulmonary fibrosis through suppressing TGF-β and SDF-1 secreted by macrophages and fibroblasts *via* the PI3K-dependent AKT and ERK pathways

Chinese Journal of Natural Medicines. 2023, 21(7), 527-539 https://doi.org/10.1016/S1875-5364(23)60444-3

New anti-pulmonary fibrosis prenylflavonoid glycosides from *Epimedium koreanum*

Chinese Journal of Natural Medicines. 2022, 20(3), 221-228 https://doi.org/10.1016/S1875-5364(21)60116-4

Dihydroartemisinin attenuates ischemia/reperfusion-induced renal tubular senescence by activating autophagy

Chinese Journal of Natural Medicines. 2023, 21(9), 682-693 https://doi.org/10.1016/S1875-5364(23)60398-X

Si-Wu-Tang attenuates liver fibrosis *via* regulating lncRNA H19-dependent pathways involving cytoskeleton remodeling and ECM deposition

Chinese Journal of Natural Medicines. 2024, 22(1), 31-46 https://doi.org/10.1016/S1875-5364(24)60560-1

A naturally derived small molecule compound suppresses tumor growth and metastasis in mice by relieving p53-dependent repression of CDK2/Rb signaling and the Snail-driven EMT

Chinese Journal of Natural Medicines. 2024, 22(2), 112-126 https://doi.org/10.1016/S1875-5364(24)60550-9

Rhodiola crenulata extract decreases fatty acid oxidation and autophagy to ameliorate pulmonary arterial hypertension by targeting inhibiton of acylcarnitine in rats

Chinese Journal of Natural Medicines. 2021, 19(2), 120-133 https://doi.org/10.1016/S1875-5364(21)60013-4

Wechat

Chinese Journal of Natural Medicines 24 (2026) 1205-1220

Contents lists available at ScienceDirect

Chinese Journal of Natural Medicines

journal homepage: www.cjnmcpu.com/



Original article

Targeting senescence-associated fibrotic signatures identifies syringin as an effective modulator of the ATR/CHK1–p53 axis in idiopathic pulmonary fibrosis

Yuyang Wang[a,b], Guanghui Yin[a,b], Mixing Niu[a,b], Wei Wang[b,c], Zhenyun Liao[b], Lei Yang[b], Chunli Wu[b], Yu Cao[d,*], Kai Gao[b,*], Zhaoxing Dong[a,b,*]

[a] *School of Public Health, Hangzhou Medical College, Hangzhou 310014, China*
[b] *Department of Respiratory and Critical Care Medicine, Ningbo No. 2 Hospital, Ningbo 315010, China*
[c] *Cixi Biomedical Research Institute, Wenzhou Medical University, Cixi 315300, China*
[d] *Department of Respiratory, The Second Affiliated Hospital of Kunming Medical University, Kunming 6500101, China*

ARTICLE INFO

Article history:
Received 3 February 2026
Revised 22 July 2026
Accepted 26 July 2026
Available online 20 October 2026

Keywords:
ATR/CHK1–p53 pathway
Idiopathic pulmonary fibrosis
Syringin
Cell senescence

ABSTRACT

Idiopathic pulmonary fibrosis (IPF) is a progressive and fatal interstitial lung disease closely associated with aging, yet the contribution of cellular senescence to fibrotic remodeling and its therapeutic implications remain incompletely understood. Syringin, a phenylpropanoid glycoside derived from *Acanthopanax senticosus*, has been reported to possess anti-inflammatory and antioxidant activities, but its role in IPF has not been elucidated. In this study, bulk lung transcriptomic data from the GTEx project and nine IPF cohorts were integrated with IPF scRNA-seq data to characterize senescence-associated fibrotic programs. A systems-level compound prioritization strategy incorporating reversed gene expression scoring, network proximity analysis, drug-likeness and toxicity evaluation was applied to identify candidate molecules. The results revealed a pronounced aging-associated transcriptomic profile in IPF lungs, with strong concordance between age-related and IPF-related gene programs. Single-cell analyses further identified senescent fibroblast populations as key cellular hubs characterized by elevated expression of SASP factors. Syringin was subsequently validated in TGFβ1–stimulated fibroblasts, and a murine model of bleomycin-induced pulmonary fibrosis. Syringin consistently attenuated fibroblast activation, cellular senescence markers, and pulmonary fibrosis *in vivo* and *in vitro*. Mechanistically, syringin markedly reversed the activation of replication stress–associated signaling pathways. Molecular docking and CETSA suggested a potential interaction between syringin and CHK1. Furthermore, CHK1 knockdown partially abrogated the regulatory effects of syringin on the ATR/CHK1–p53 signaling cascade, supporting CHK1 as a functional mediator of syringin activity. Collectively, these findings identify syringin as a natural small molecule with anti-senescent and anti-fibrotic properties, and may represent a potential therapeutic strategy for IPF.

1. Introduction

Idiopathic pulmonary fibrosis (IPF) is a lethal interstitial lung disease characterized by progressive, irreversible lung tissue remodeling and scarring, with a complex pathogenesis and extremely poor clinical prognosis [1]. Although antifibrotic drugs such as pirfenidone and nintedanib have been approved for clinical use, their efficacy primarily manifests in slowing the decline of lung function. They remain unable to reverse established fibrotic pathological changes, and the median survival of patients remains significantly limited [2, 3]. This therapeutic bottleneck indicates that existing intervention strategies have yet to effectively target the core cellular processes and molecular hubs driving the persistent progression of IPF. There is an urgent need to identify key mechanisms and therapeutic targets for intervention from new pathological dimensions.

In recent years, cellular senescence has increasingly been recognized as an important biological basis for the occurrence and progression of IPF [4]. Several studies have demonstrated that lung tissue from IPF patients commonly exhibits telomere shortening [5], accumulated DNA damage [6], upregulation of cell cycle suppressor proteins (such as p21 and p16) [7], and enhanced senescence-associated secretory phenotype (SASP) [8]. These findings suggest that IPF possesses a distinct molecular phenotype characterized by accelerated aging. However, existing studies have primarily focused on phenomenological level descriptions, lacking systematic evidence to elucidate whether the aging program is positioned upstream in the IPF disease cascade and directly drives the formation and maintenance of the fibrotic phenotype. Meanwhile, the relative contributions of different types of lung cells to aging signals and their functional localization within the disease microenvironment remain unclear, which somewhat limits the feasibility of translating senescence-associated mechanisms to therapeutic targets.

* Corresponding author.
E-mail addresses: caoyuyisheng@163.com (Y. Cao); gaokai@bucm.edu.cn (K. Gao); dongkm@hotmail.com (Z. Dong)

https://doi.org/10.1016/S1875-5364(26)61215-0
Copyright © 2026, China Pharmaceutical University. Published by Elsevier B.V. All rights are reserved.

Fibroblasts are the central effector cells responsible for abnormal extracellular matrix deposition and scar formation in IPF [9]. Previous studies have demonstrated that IPF pulmonary fibroblasts exhibit not only persistent activation but also a characteristic senescence-like phenotype [10]. While their proliferative capacity is limited, they continuously secrete multiple pro-fibrotic and pro-inflammatory factors, thereby sustaining and amplifying the pathological microenvironment [11]. However, the systematic molecular features of the fibroblast senescence program and its coupling with classical fibrosis signaling pathways have yet to be fully resolved.

Based on the aforementioned scientific questions, this study systematically analyzes the molecular characteristics and cellular ecology underlying the pulmonary tissue aging program in IPF, with a particular focus on key regulatory pathways linking fibroblast senescence to the fibrotic phenotype. By integrating multi-cohort transcriptomic data with single-cell sequencing data, this study systematically identified highly consistent transcriptomic signatures between IPF and pulmonary aging, confirming fibroblasts as the core cell type in which aging programs are abnormally activated. Furthermore, focusing on the drug-targeting potential of the "senescence-fibrosis" coupling mechanism, this study established a multidimensional screening system for traditional Chinese medicine small molecules. We identified syringin as a candidate molecule that simultaneously inhibits both fibroblast senescence and fibrosis phenotypes. Mechanistic studies indicate that syringin regulates aging programs associated with DNA damage response by inhibiting the activity of the ATR/CHK1–p53 signaling axis, thereby achieving dual intervention in the pathological state of fibroblasts.

2. Materials and methods

2.1. Public transcriptomic datasets

Bulk transcriptomic profiles of normal human lung tissue were obtained from the Genotype-Tissue Expression (GTEx) project [12]. IPF-related bulk RNA-seq datasets were collected through a systematic search of the DiSignAtlas [13] and Gene Expression Omnibus (GEO) databases [14]. Datasets were included if they met the following criteria: (i) human lung tissue or lung-derived cells; (ii) inclusion of both IPF and healthy control samples; (iii) availability of raw sequencing count data; (iv) a minimum of three samples per group; and (v) absence of pharmacological interventions, acute inflammatory models, or complex disease backgrounds. Based on these criteria, nine independent IPF cohorts comprising more than 330 samples were included. Single-cell RNA sequencing (scRNA-seq) data were obtained from GEO (GSE132771), generated using the 10x Genomics platform and including lung tissue samples from IPF patients and matched healthy controls.

2.2. Data preprocessing and normalization

Bulk RNA-seq data were filtered to remove low-abundance genes (retained if expressed in at least three samples) and normalized using the size-factor method implemented in DESeq2. Given the multi-cohort nature of the IPF datasets, batch effects were assessed and corrected using ComBat-seq. The effectiveness of batch correction was evaluated by principal component analysis before and after adjustment.

For scRNA-seq data, stringent quality control criteria were applied to remove low-quality cells, high mitochondrial content cells, and potential doublets through DoubletFinder [15]. Data normalization, identification of highly variable genes, scaling, and batch correction were performed using Seurat in combination with Harmony [16], ensuring consistency in downstream clustering and cell type annotation across samples.

2.3. Differential expression and aging-associated signature construction

To characterize age-associated transcriptional changes in the lung, DESeq2 was used to construct multivariable linear models in the GTEx dataset, with age as the primary explanatory variable and sex and RNA integrity as covariates. Differentially expressed genes were identified across multiple age group comparisons, and genes exhibiting consistent directional changes across at least three comparisons were defined as the core lung senescence gene set.

IPF-associated differential expression analyses were conducted at both bulk and single-cell levels. For bulk RNA-seq data, differential expression between IPF and control samples was determined using normalized and batch-corrected count matrices. At the single-cell level, the MAST framework was applied within annotated cell populations while controlling for potential confounders.

The overlap and concordance between aging- and IPF-related gene programs were quantified using Fisher's exact test, odds ratios, Jaccard indices, and gene set enrichment analysis.

2.4. Single-cell senescence scoring

At the single-cell level, senescence activity and senescence-associated secretory phenotype (SASP) scores were calculated using AUCell based on the core lung senescence gene set and IPF–senescence overlapping signatures.

Fibroblasts were selected as the primary cell type of interest and further stratified into senescent and non-senescent subpopulations according to SASP activity. Differentially expressed genes between these subpopulations were identified to characterize senescence-associated transcriptional programs.

2.5. Functional enrichment and cell–cell communication analysis

Gene Ontology (GO) and pathway enrichment analyses were performed using the clusterprofile [17]. The GO analysis encompassed three categories: biological process (BP), cellular component (CC), and molecular function (MF). Enrichment significance was assessed *via* hypergeometric tests and corrected using the Benjamini–Hochberg method ($q < 0.05$).

Pathway activity scores for aging-related, IPF–senescence overlapping, and SASP-related pathways were calculated at the single-cell level using AUCell, and differences between IPF and control samples were statistically evaluated.

To investigate intercellular communication patterns, CellChat [18] was used to infer ligand–receptor interactions and signaling pathway networks in normal and IPF lungs. Centrality analysis was performed to identify key cell types contributing to senescence-associated fibrotic signaling.

2.6. Small-molecule screening and prioritization

Active TCM small-molecule constituents and their RNA-seq profiles were retrieved from the ITCM database [19], and small molecule-target associations were extracted from HERB 2.0 [20]. The IPF & Aging signature gene set (110 consistent feature genes) was constructed by intersecting age-related DEGs (GTEx database) with IPF cohort DEGs and enforcing consistent expression regulation directions, based on multi-omics integration results and shared IPF-pulmonary senescence pathological features.

Candidate efficacy was validated *via* a dual-algorithm approach: (1) the Reverse Gene Expression Signature (RGES) al-

gorithm [21] for vector matching between 496 small-molecule RNA-seq profiles and the IPF & Aging signature; (2) Network Proximity algorithm [22] to calculate topological distances between small-molecule target sets and disease core gene sets, using a high-confidence STRING-derived PPI network [23].

Innovation and safety evaluations included: (1) PubMed search (up to June 1, 2024) prioritizing candidates with confirmed anti-aging evidence but no reported anti-pulmonary fibrosis activity; (2) QED scoring (RDKit-calculated parameters) for drug-likeness; (3) ADMETlab 2.0 [24] assessment retaining candidates with low respiratory toxicity.

A stepwise screening pipeline integrating six dimensions (RGES reversal potential, PPI network proximity, anti-aging/anti-pulmonary fibrosis research status, QED properties, respiratory toxicity) was established to identify top candidates for subsequent *in vitro* and *in vivo* validation.

2.7. Experimental materials and reagents

Syringin (Catalog No. T3024, purity 99.56%) was purchased from TargetMol; ATR inhibitor VE-822 (Catalog No. S7102, purity 99.77%) was purchased from Selleck (https://www.selleckchem.com/); Bleomycin sulfate (purity 98.0%) was purchased from CSNpharm; Recombinant TGF-β1 protein was purchased from Novoprotein; CCK-8 assay kit was purchased from ApexBio; SA-β-GAL staining kit was purchased from Beyotime; Total RNA extraction kit purchased from ONREW; Reverse transcription kit and SYBR Green I qPCR kit purchased from Takara; Collagen I (Col1a1), TGF-β, α-SMA, GAPDH primary antibodies, and HRP-conjugated secondary antibodies purchased from Abcam; RIPA lysis buffer, protease-phosphatase inhibitor mixture, and SDS-PAGE gel preparation kit were purchased from Epizyme; ECL chemiluminescent substrate was purchased from NCM; PVDF membranes were purchased from Millipore; other routine chemical reagents were all analytical grade.

2.8. Animal and experimental models of pulmonary fibrosis

Forty male C57BL/6 mice, 8 weeks old, weighing 20 ± 2 g, and free from specific pathogens were provided by Zhejiang Vital River Laboratory Animal Technology Co., Ltd. (Hangzhou, China). All animal procedures were performed according to the National Institutes of Health Guide for the Use of Laboratory Animals with approval from the Animal Care and Use Committee of Ningbo Institute of Life and Health Industry (GK-2025-XM-0143).

After a 7-day adaptive feeding period, the mice were stratified by body weight to ensure equal weight distribution across groups. Subsequently, using a simple random number method implemented, they were randomly assigned to five groups (n = 8): Control, BLM, BLM + SG-H, BLM + SG-M, and BLM + SG-L. On Day 0, the animals were anesthetized with isoflurane. The BLM group, BLM + SG-H group, BLM + SG-M group, and BLM + SG-L group received a single intratracheal instillation of bleomycin sulfate (3 mg·kg^{-1}), while the control group received an equivalent volume of sterile saline. The selection of a dose of 3 mg·kg^{-1} is based on previous studies, as it is sufficient to induce replicable pulmonary fibrosis while minimizing mortality and reducing unnecessary animal suffering [25]. Animals undergo a 12 h light/dark cycle at a controlled temperature of (22 ± 3 °C). To simulate the therapeutic intervention model, we started the treatment from the first day after BLM administration. The BLM + SG-H group, BLM + SG-M group, and BLM + SG-L group were respectively given syringin (40 mg·kg^{-1}·d^{-1}, 20 mg·kg^{-1}·d^{-1}, 10 mg·kg^{-1}·d^{-1}, gavage) for 21 consecutive days. Mice in the BLM group and the control group were given with the same volume of normal saline according to the same procedure. On the 21st day, the animals were sacrificed and the lung tissues were preserved at −80 °C for further analysis.

2.9. Cell culture and treatment

The mouse embryonic fibroblast cell line NIH/3T3 and the human fetal lung fibroblast cell line MRC-5 were both purchased from Zhejiang Ruyao Biotechnology Co., Ltd. (Ningbo, China). The pulmonary fibrosis model was constructed by incubating approximately 60% fused cells in low-serum medium for 12 h and then stimulating them with TGF-β1 for 24 h. The cells were further incubated in complete culture medium containing different concentrations of syringin for another 24 h. The replication stress senescence model was constructed by incubating ~60% fused cells in low-serum medium for 12 h and then adding BLM for stimulation for 24 h. Meanwhile, under the same conditions, 1 μmol·L^{-1} ATR inhibitor VE-822 was added for pathway inhibition experiments.

2.10. Cell viability and proliferation assays

The cell activity after treatment with syringin was evaluated by the CCK-8 method. NIH/3T3 cells were seeded in 96-well plates and adhered overnight. The next day, fresh culture medium containing 0, 5, 10, 20, 30, 40, 50, 75, and 100 μmol·L^{-1} of syringin was used instead of the culture medium. After incubation for 24 h, a mixed solution of 10 μL of CCK-8 and 100 μL of complete culture medium was added to each well. Incubate at 37 °C with 5% CO_2 for 4 h, away from light.

To conduct proliferation analysis under fibrotic stimulation, NIH/3T3 cells were seeded in 96-well plates. After cell adhesion (~ 4–6 h), the cells were treated with complete culture medium containing TGF-β1 (10 ng·mL^{-1}) for 24 h, and then treated with different concentrations of syringin or fresh culture medium for 24 h. Absor Bance read at 450 nm using an Epoch 2 microplate reader and calculated the survival rate as a percentage of the untreated control. Each experiment was independently repeated six times.

2.11. Lung histopathology

Lung tissue specimens were fixed with 4% paraformaldehyde (Wuhan, China), embedded in paraffin, and sectioned in 4-μm sections. After dewaxing, ethanol staged dehydration and rehydration, lung sections were stained with hematoxylin-eosin (H&E) and Masson's tricolor staining. Histological changes were observed using the eclipse Ni-E upright microscope (Nikon, NY, USA) within the randomly selected histological field, and analyzed using ImageJ software, including Ashcraft score (0–8 grades) and the determination of the positive area of collagen.

2.12. Western blot assay

Lung tissue or whole cell lysate was lysed on ice for 30 min in a mixture containing RIPA and protease-phosphatase inhibitors, then extracted by centrifugation. The protein samples were separated by SDS-PAGE, followed by transfer to PVDF membrane. The PVDF membrane was blocked with rapid blocking solution for 15 min, then incubated overnight with the primary antibody at 4 °C. Subsequently, incubation with HRP-conjugated secondary antibody (1∶20 000, Abcam) was carried out at room temperature for 60 min. Detection of protein bands specifically bound to the primary antibody was achieved using ECL substrate. Band intensity was quantified using ImageJ software, normalized to GAPDH, and the phosphorylated protein level was presented as a ratio to the total protein. Data were expressed as relative optical density, with each dataset replicated at least three times.

2.13. RT-PCR

RNA was isolated with the high-purity RNA extraction kit (Full Gold, Beijing) and quantified using the Thermo nanodrop one ultramicro spectrophotometer. For cDNA synthesis, 1 μg of total RNA was employed following the manufacturer's protocol with the reverse transcription kit (Full Gold, Beijing). Gene amplification was carried out using the SYBR GreenI polymerase chain reaction master kit (Full Gold) and the qTOWER3 fluorescence quantitative gene amplification instrument. The relative expression levels of the target genes were normalized to GAPDH using the $2^{-\Delta\Delta Ct}$ method.

2.14. Immunohistochemistry

Immunohistochemistry involved preparing 4-μm formalin-fixed paraffin-embedded tissue sections, dewaxing with xylene, and rehumidifying with ethanol. Antigen retrieval in EDTA buffer (pH 8.0) was done by microwave heating. Sections were treated with 3% hydrogen peroxide at room temperature for 10 min, then blocked with normal serum for 30 min. Primary antibodies (Col1a1, TGF-β, α-SMA) at 1∶200 dilution were incubated overnight at 4 °C in 10% bovine serum albumin. Protein detection was done using 3,3'-diaminohydrazine staining, with hematoxylin for nuclear staining. Stained sections were examined under an optical microscope, capturing images with consistent settings. ImageJ was used to quantify the average optical density (MOD) of positive staining for each target.

2.15. Immunofluorescence assay

In the multiplex fluorescence staining experiment, the assay was performed using the multiplex fluorescent immunohistochemistry staining kit from Absin Biotechnology Co., Ltd. The detailed procedure involved sample fixation, permeabilization (for intracellular antigens), and blocking of endogenous peroxidase activity. This was followed by sequential incubation with primary antibodies (at 4 °C overnight or at 37 °C for 1–2 h) and corresponding HRP-conjugated secondary antibodies, with signal amplification achieved using tyramide signal amplification (TSA) dyes. For multi-target detection, an antibody elution buffer (applied at 37 °C for 15–30 min) was used to remove signals from previous rounds before repeating the aforementioned steps for subsequent staining. Finally, nuclei were counterstained with DAPI, and the samples were mounted with anti-fade mounting medium prior to scanning and imaging.

2.16. Hydroxyproline assay

Tissue hydroxyproline levels were measured using the hydroxyproline assay Kit from Nanjing Jiancheng Institute of Bioengineering. Oxidation products from hydroxyproline, when exposed to oxidizing agents, react with dimethylaminobenzaldehyde, resulting in a purple-red hue. Hydroxyproline concentration is determined by the intensity of this color. Following kit instructions, 1 mL of hydrolyzed solution was added to 30 to 1000 mg of tissue, hydrolyzed at 95 °C for 20 min, pH adjusted to approximately 6.0 to 6.8, supplemented with water and activated carbon, thoroughly mixed, centrifuged to collect the supernatant, measured at 550 nm, and quantified. Each dataset was replicated at least thrice.

2.17. RNA-sequencing and bioinformatics analysis

RNA sequencing analysis was performed on NIH/3T3 cells from the control, model, and SG groups. Sequencing was conducted by Shanghai Personal Biotechnology Co., Ltd. (Shanghai, China). Raw data in Fastq format were initially preprocessed using Fastp software. After gene annotation, gene counting was carried out with StringTie, followed by differential expression analysis across groups using the edgeR to identify differentially expressed genes.

2.18. SA-β-gal staining

Cell senescence was detected using the SA-β-GAL kit. The staining protocol followed the manufacturer's instructions. After removing the cell culture medium from 6-well plates, cells were washed with PBS, fixed with β-galactosidase staining fixative for 15 min at room temperature. Subsequently, the fixative was removed, and cells were washed thrice with PBS for 3 min each. Staining working solution (1 mL) was added to each well, followed by overnight incubation at 37 °C. Images were captured using a microscope (Leica DMi1) equipped with a digital camera. At least three fields of view were captured per image to quantify SA-β-GAL staining intensity.

2.19. Molecular docking

Molecular docking was performed to explore the potential interactions between Syringin and candidate target proteins. The crystal structures of checkpoint kinase 1 (CHK1, PDB ID: 3TKI) and ataxia telangiectasia and Rad3-related kinase (ATR, PDB ID: 9L40) were retrieved from the Protein Data Bank (https://www.rcsb.org/) [26]. Protein structures were prepared using AutoDockTools (version 1.5.7) by removing water molecules and heteroatoms, followed by addition of polar hydrogens and assignment of Gasteiger charges [27]. The 3D structure of Syringin was obtained from PubChem (https://pubchem.ncbi.nlm.nih.gov/) and prepared using the same software, with rotatable bonds defined prior to docking.

Docking simulations were carried out using AutoDock Vina with a semi-flexible docking protocol. The docking grid box was defined to cover the predicted active pocket of each protein, and default parameters were used unless otherwise specified. The binding conformation with the lowest predicted binding free energy was selected for further analysis [28]. Docking complexes were visualized using PyMOL (version 3.1.82). Protein–ligand interaction profiles, including hydrogen bonds and hydrophobic contacts, were analyzed using LigPlot + (version 2.3) and the PLIP web server [29].

2.20. Cellular thermal shift assay (CETSA)

NIH/3T3 cells were treated with SG or the control compound DMOG for 2 h. Following treatment, cells were harvested and resuspended in PBS containing protease inhibitors. The cell suspension was aliquoted into PCR tubes and exposed to a temperature gradient ranging from 35 to 70 °C for 3 min, followed by cooling at room temperature for 3 min. Cells were subsequently lysed by repeated liquid nitrogen freeze-thaw cycles. The lysates were centrifuged at 15 000 $r \cdot min^{-1}$ for 20 min at 4 °C, and the supernatants (soluble protein fractions) were collected. Target protein levels were quantified by Western blotting, with band intensities normalized to the signal at 37 °C (set as 100%). Melting curves were plotted and analyzed using GraphPad Prism.

2.21. siRNA knockdown experimental methods

Small interfering RNA targeting mouse CHK1 (siCHK1) and a negative control siRNA (si-NC) were designed and synthesized by Magi Biotechnology (China). NIH/3T3 cells were cultured in high-glucose DMEM supplemented with 10% fetal bovine serum and

1% penicillin/streptomycin at 37 °C in a humidified incubator containing 5% CO_2. Twenty-four hours prior to transfection, cells were seeded into 12-well plates to achieve approximately 60%–70% confluence at the time of transfection. Transfection was performed according to the recommended concentration and protocol provided by the Yaseyue transfection reagent kit. Twenty-four hours after transfection, cells were harvested, and CHK1 mRNA expression levels were detected by qRT-PCR, while CHK1 protein expression levels were examined by Western blot to evaluate knockdown efficiency. Subsequent experiments were performed 48–72 h after transfection.

2.22. Statistical analysis

All bioinformatics analyses were performed in the R 4.3.1 environment. All the analyses of the experiments were repeated by at least three organisms. All values are expressed as the mean ± SD. The experimental data were analyzed using one-way ANOVA and Tukey's multiple comparisons. Statistical analysis was performed using GraphPad Prism 9.0 (GraphPad Software, USA).

3. Results

3.1. GTEx lung tissue transcriptome analysis reveals age-related molecular characteristics

Based on the GTEx (v10) database, this study constructed a lung tissue age gradient transcriptome map covering the age range of 20 to 79 years old. A total of 604 lung tissue samples were included (Fig. 1A). The age distribution covered six intervals from 20–29 years old to 70–79 years old. The samples of middle-aged people (40–59 years old) and the elderly (60–69 years old) accounted for the highest proportion (about 83%).

Using the 20–29 years age group as the baseline, pairwise differential expression analysis was performed on the remaining five age groups, revealing that lung tissue transcriptomes undergo significant age-dependent dynamic changes. The number of differentially expressed genes (DEGs) increased markedly with age (Fig. 1B): only 43 significant DEGs were detected in the 30–39 years group (*FDR* < 0.05), whereas this number surged to 598 in the 60–69 years group (13.9-fold higher than the former). The 70–79 years group still retained 422 DEGs, indicating that lung tissue gene expression exhibits a characteristic of progressive reprogramming during aging. Both upregulated and downregulated DEG counts displayed a synchronous increasing trend, with a high degree of directional consistency observed in the elderly cohort (60–69 years), which reflects the continuous molecular trajectory underlying lung tissue aging.

To identify the most representative molecular characteristics of aging across age gradients, we integrated genes with consistent expression directions (≥ 3 groups of co-directional changes) in each age comparison to construct the core lung aging gene set. Ultimately, 335 core up-regulated genes and 202 down-regulated genes were obtained (Figs. 1C and 1D), representing stable molecular markers accumulated in lung tissue with age.

Functional enrichment analysis revealed that the core upregulated genes were mainly concentrated in extracellular matrix (ECM) remodeling, mechanical stress response, immune and inflammatory regulation, and oxidative stress pathways. The core down-regulated genes are enriched in processes such as cell proliferation and repair, DNA damage response, and lung differentiation and development. These characteristic pathways are highly consistent with the known molecular mechanisms of IPF, suggesting that lung aging may be an important molecular background for the occurrence of IPF.

3.2. Systematic integration analysis of lung aging characteristics and IPF transcriptome

To systematically evaluate the overall activation status of pulmonary senescence programs in IPF, this study integrated and analyzed the IPF bulk RNA-seq cohorts from 9 independent studies, involving a total of 330 lung tissue samples. Principal component analysis (PCA) before integration showed that the samples were mainly clustered by research source in the principal component space, suggesting significant batch effects among different cohorts (Fig. 2A). After batch correction by ComBat-seq, the cohort separation between samples was significantly weakened, indicating that the batch effect was effectively controlled. The corrected data can be used for robust cross-cohort biological comparisons.

In the corrected integrated cohort, a total of 1520 IPF up-regulated genes and 821 down-regulated genes were identified (Figs. 2B, 2C, and 2D). The intersection analysis of the core lung aging gene set constructed by GTEx and the IPF differential genes showed a highly significant direction-specific overlap. Among the 27 685 background genes, the intersection of 335 core age-up-regulated genes and IPF-upregulated genes reached 101. In contrast, the intersection of 202 core age-down-regulating genes with IPF-down-regulating genes was only 9. The UpSet graph further shows that this overlap is almost entirely driven by the directionally consistent combination of "age upregulation–IPF upregulation", while the cross-directional overlap is close to zero, suggesting a highly directionally consistent coupling relationship between the lung aging program and the IPF molecular phenotype.

The above-mentioned directional overlap also shows extremely strong significance at the statistical level. The odds ratio (OR) of the "age upregulation–IPF upregulation" combination was as high as 7.887 ($P = 5.06 \times 10^{-47}$), and the Jaccard index was 0.058, indicating an enrichment intensity far exceeding the random expectation. The OR of the "age reduction–IPF reduction" combination was 1.532 ($P = 0.207$), and the *Jaccard index* was only 0.009, not reaching the statistically significant level. This result indicates that the activated molecular programs in IPF are highly enriched in the aging upregulated gene set that gradually intensifies in lung tissue with age, while the aging-related down-regulated programs do not show a symmetrical inhibitory pattern in IPF.

To further quantify the overall association between age effects and IPF effects at the genetic level, the median $\log_2$FC of each gene in the GTEx age gradient and its $\log_2$FC in the IPF cohort were constructed and a correlation analysis was conducted (Fig. 2E). Across the entire gene range, the two show a weak but significant positive correlation. In the core aging gene set, this correlation is significantly enhanced, indicating that this gene set has higher consistency in the two biological scenarios. The top 10 genes with the most prominent bidirectional effects (including immunoglobulin family members such as *IGHG4*, *IGHV1-69D*, and structural molecules like *COL10A1*, *COMP*) are primarily involved in humoral immune response and extracellular matrix organization, which further supports their potential key role in mediating the "senescence-fibrosis" axis (e.g., immune dysregulation and matrix homeostasis imbalance).

GSEA analysis was conducted based on the list of IPF differentially expressed genes sorted by $\log_2$FC, further verifying the systematic activation of the core lung aging program in IPF (Fig. 2F). The enrichment curve shows that the core aging genes are significantly concentrated at the high-expression end of the sequencing list, with a significantly increased standardized enrichment score (NES) and a significant adjusted *P*-value, indicating that this gene set is one of the strongest functional enrichment modules in the IPF full transcriptome.

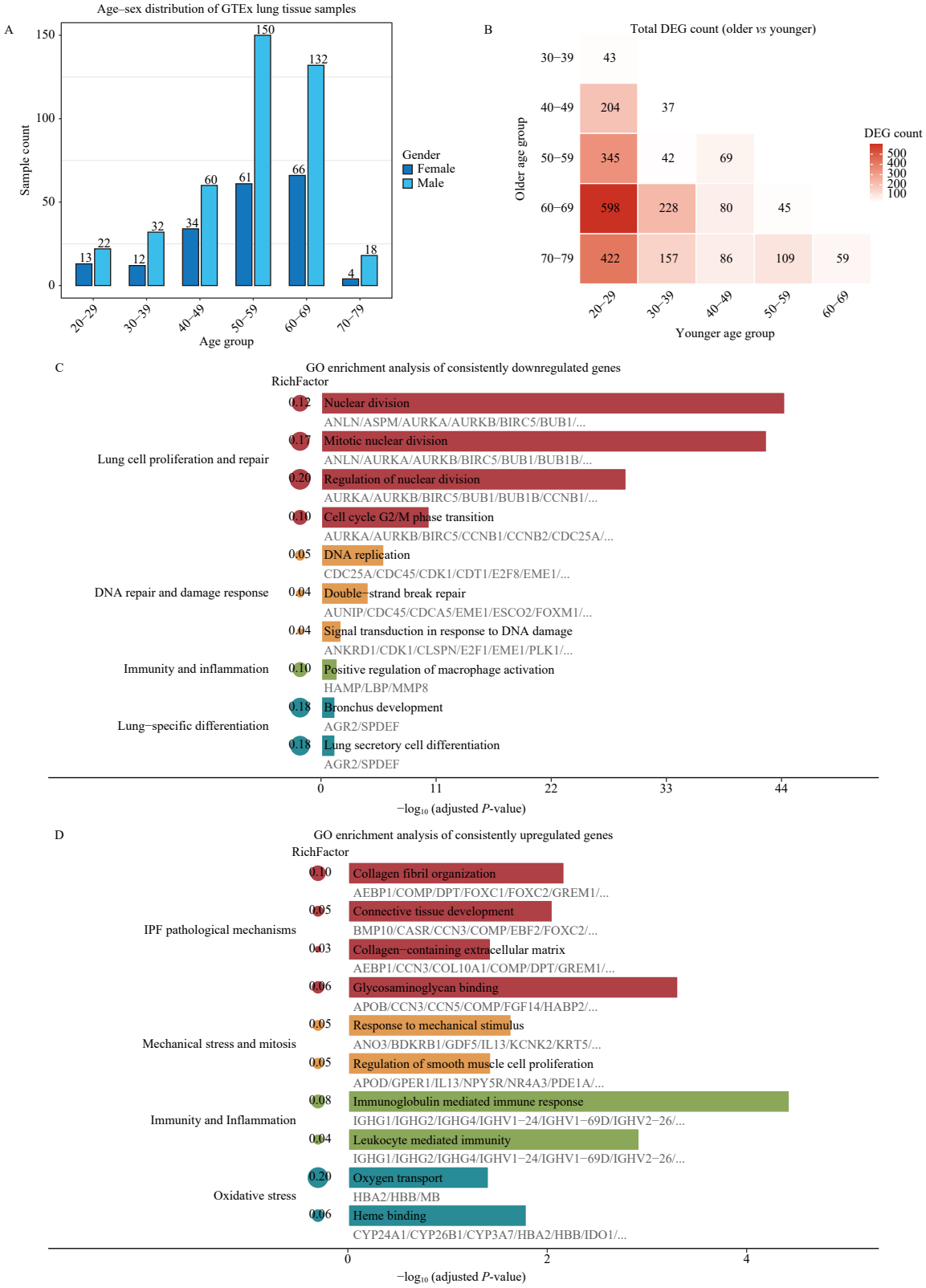


Fig. 1 Analysis of age-related transcriptomic features in human lung tissue based on the GTEx database. (A) Compositional distribution of lung tissue samples across different age groups. (B) Heatmap of differentially expressed genes by age group. (C) GO biological process enrichment analysis of the core downregulated lung aging gene set (202 genes consistently downregulated). (D) GO biological process enrichment analysis of the core upregulated lung aging gene set (335 genes consistently upregulated).

In conclusion, the multi-cohort integrated analysis consistently revealed that the molecular modules that are upregulated with age in the lung aging program are significantly and systematically activated in the IPF, while the down-regulation program of aging does not show corresponding inhibition. This result provides direct and strong evidence for the hypothesis that "excessive activation of the aging program drives the pathological progression of IPF" at the transcriptome level of human lung tissue.

3.3. Single-cell level analysis of the cellular mechanisms of lung senescence programs in IPF

To clarify the main cellular sources and target sites of lung aging programs in IPF, this study systematically analyzed the

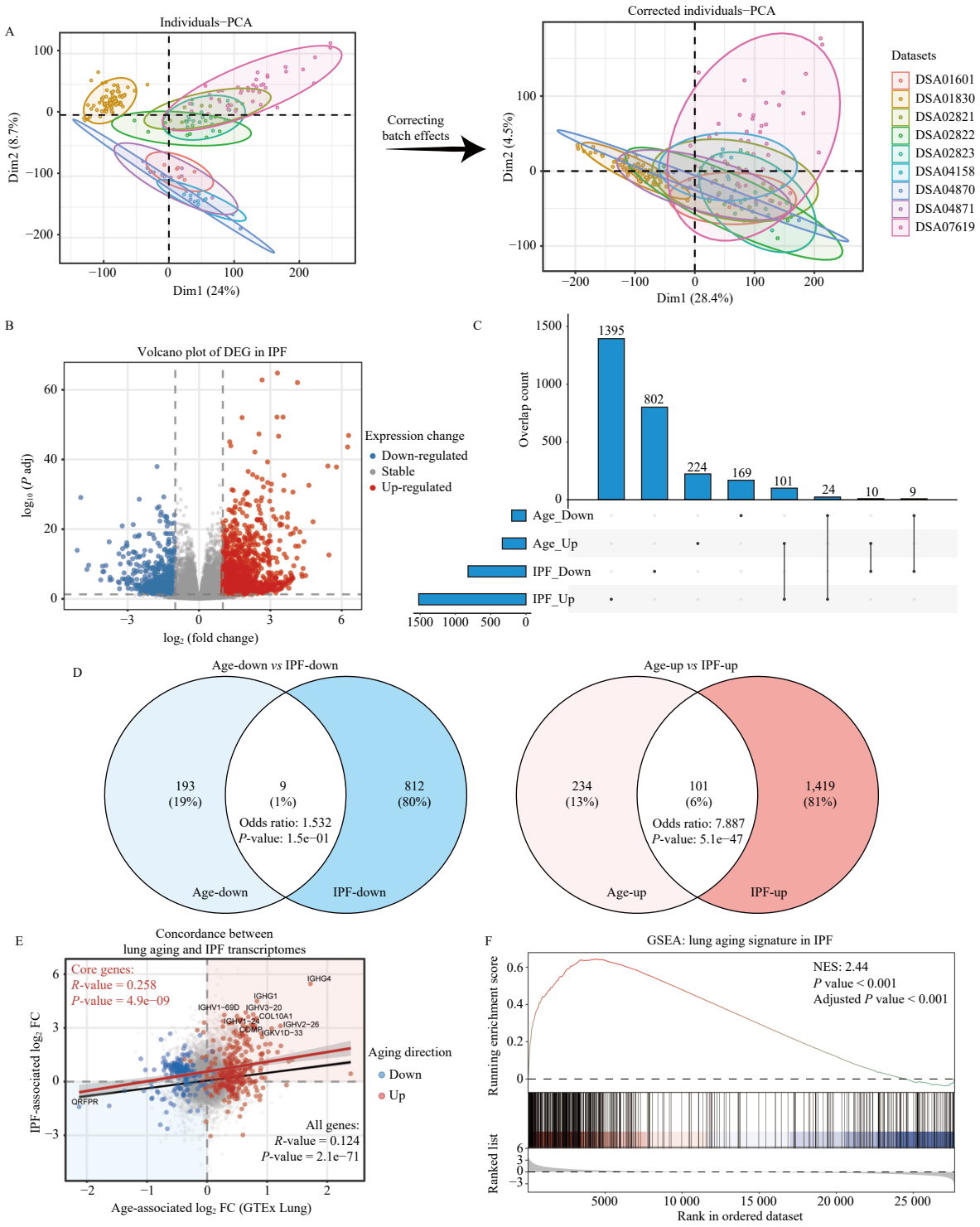


Fig. 2 Systematic Association Analysis of IPF Molecular Features and Lung Aging Program. (A) Batch effect removal efficacy across 9 IPF RNA-seq cohorts, principal component analysis (PCA) plot. (B) Volcano plot of differentially expressed genes between IPF and normal lung tissue after batch correction. (C) Upset plot of IPF differentially expressed genes and core genes of lung aging, showing intersecting gene counts. (D) Venn diagram illustrating expression direction consistency overlap between core aging genes and IPF differentially expressed genes. (E) Scatterplot correlating core gene log_2FC across GTEx age gradient with IPF log_2FC. (F) GSEA based on IPF-ranked gene list, demonstrating significant enrichment and overall activation of core aging programs in IPF.

scRNA-seq data of lung tissues from 3 IPF patients and 3 normal controls in the GEO dataset GSE132771.Based on unsupervised clustering and classical marker gene annotation, a total of 16 major cell types were identified (Fig. 3A), including alveolar macrophages, classical monocytes, vascular endothelial cells, alveolar fibroblasts, alveolar epithelial cells, and various immune and interstitial cells. The Top 5 marker genes of each cell type were displayed through heat maps (Fig. 3B), verifying the accuracy and consistency of cell annotation.

Cell composition analysis revealed significant differences in cell proportion and spatial distribution between the IPF group and the normal group (Fig. 3C). Compared with normal lung tissue, the proportion of alveolar macrophages and classical monocytes in IPF samples was significantly reduced. tSNE visualization further shows that IPF and normal samples are significantly separated in low-dimensional space, especially the distribution differences of fibroblast and epithelial cell populations are most prominent (Fig. 3D), suggesting that these two types of cells may

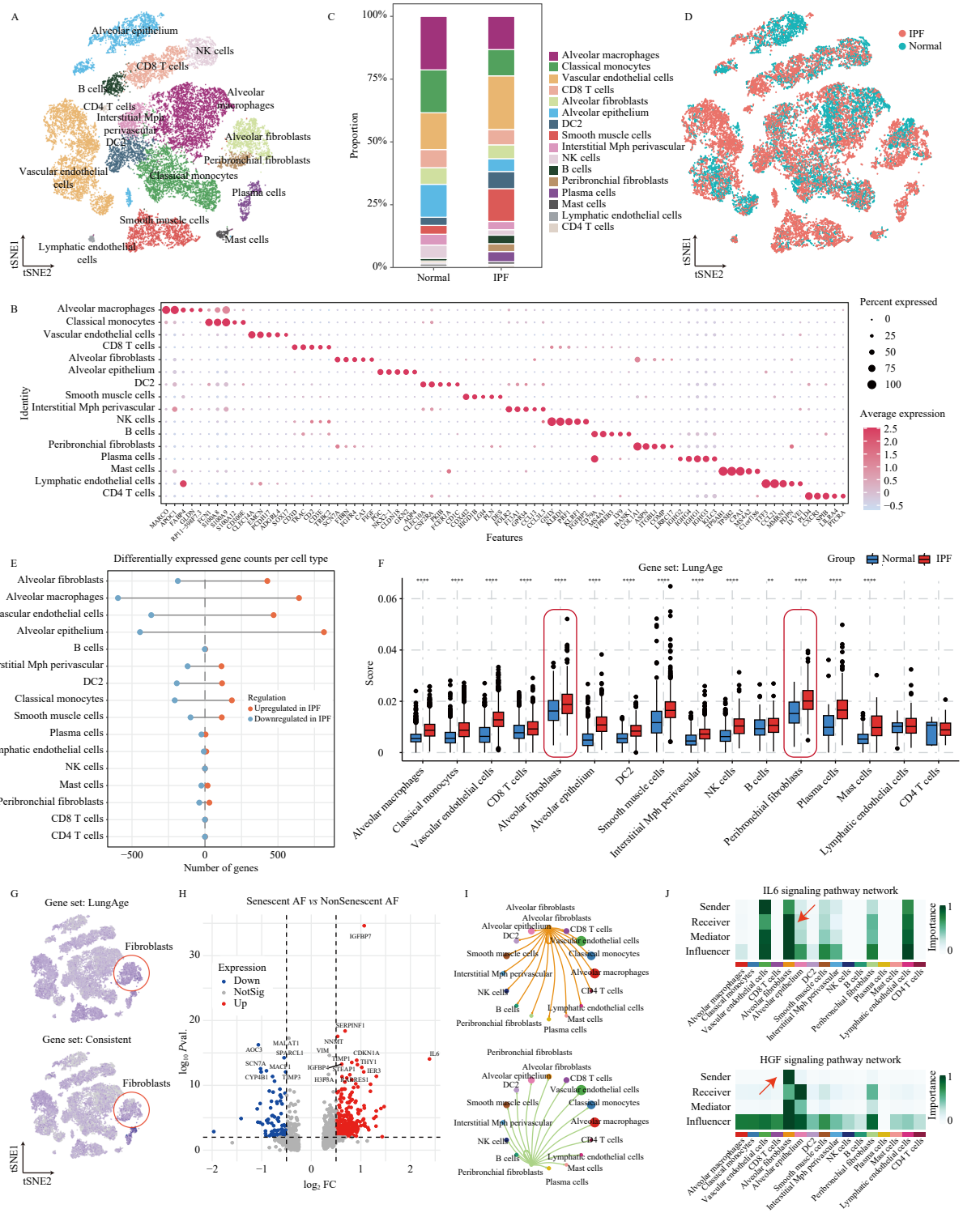


Fig. 3 ScRNA-seq reveals key cell types in lung aging and functional abnormalities in IPF. (A) TSNE plot of scRNA-seq clusters from IPF and normal lung tissues, identifying 16 cell types. (B) Heatmap of top 5 marker gene expression across 16 cell types. Rows: cell type; columns: gene. (C) Stacked bar chart showing proportion changes of each cell type between IPF and normal lung tissues. (D) TSNE space visualization of overall distribution differences between IPF and normal lung cells. (E) Comparison of IPF-associated differentially expressed genes across 16 cell types. (F) AUCell scores (quantifying senescence levels per cell type) based on core senescence gene sets. (G) TSNE plot showing senescence score distribution patterns in single-cell space. (H) Volcano plot of differentially expressed genes between "senescent" and "non-senescent" subpopulations of alveolar fibroblasts (grouped by SASP scores). (I) CellChat-constructed intercellular communication network in IPF lung tissue, with node size representing cell abundance. (J) Heatmap of cell communication patterns for key signaling pathways (IL6, HGF), showing sender-receiver pair strengths.

play a key functional role in the pathological process of IPF.

On this basis, differential expression analyses were conducted on 16 cell types respectively (Fig. 3E). The results show that alveolar epithelial cells have the largest number of differentially expressed genes, followed by alveolar macrophages and alveolar fibroblasts. However, the number of differentially expressed genes in NK cells, CD4 T cells and CD8 T cells is extremely small. This result indicates that the main molecules of IPF are abnormally concentrated in epithelial cells, fibroblasts and innate immune cell populations, which may carry the most significant aging-related transcriptional reprogramming.

To identify key cellular sources of the senescence program, AUCell was employed to calculate senescence scores at the single-cell level based on a core lung senescence gene set (Fig. 3F). Res-

ults revealed that airway fibroblasts and peribronchial fibroblasts exhibited the highest senescence scores, which were significantly elevated in the IPF group compared to the normal group. Enrichment distributions in tSNE space further confirmed that senescence-related genes were highly concentrated in the IPF fibroblast population (Fig. 3G), indicating that fibroblasts represent the core cell type abnormally activated in the pulmonary aging program during IPF.

Further, with alveolar fibroblasts as the research focus, they were classified into the "senescent subgroup" and the "non-senescent subgroup" based on the median SASP score. Differential expression analysis (Fig. 3H) revealed that genes such as *IL6*, *IGFBP7*, and *SERPINF1* in the senescent subpopulation were significantly upregulated. These genes are widely involved in inflammatory response, extracellular matrix remodeling, and cellular senescence regulation, suggesting that alveolar fibroblasts in IPF have undergone significant "senior-like reprogramming". And it may promote the fibrosis process by secreting the SASP factor.

To further explore the mechanism of senescent fibroblasts in the regulation of the IPF microenvironment, a cellular communication network between IPF and normal lung tissue was constructed based on CellChat. The results show (Fig. 3I) that airway fibroblasts have the strongest communication intensity with vascular endothelial cells and alveolar macrophages, while perbronchial fibroblasts mainly interact closely with smooth muscle cells and alveolar epithelial cells. Further analysis of the key signaling pathways (Fig. 3J) revealed that in the IL6 pathway, alveolar fibroblasts act as the main signal receivers, while vascular endothelial cells are the main signal transmitters. In the HGF pathway, alveolar fibroblasts transform into the main signal transmitters, while alveolar epithelial cells act as strong signal receivers.

The above communication mode suggests that fibroblasts may form a closed-loop regulatory node of "inflammation-senescence-fibrosis" in IPF: on the one hand, they enhance their own senescence phenotype by receiving inflammatory signals; on the other hand, they regulate the function of epithelial cells by secreting factors such as HGF, thereby stabilizing and amplifying the fibrotic microenvironment.

3.4. Multi-dimensional integrated screening system for identifying candidate small molecules of traditional Chinese medicine against IPF

To accurately identify the active ingredients of traditional Chinese medicine that can simultaneously reverse the core molecular characteristics of IPF and lung senescence, this study constructed a multi-dimensional and progressive small molecule comprehensive screening system. This system takes "functional reversal ability - disease network proximity - prior research evidence - drug-like and safety prediction" as the four core assessment dimensions (Fig. 4A), achieving a systematic and multi-level quantitative assessment of the intervention potential of small molecules in traditional Chinese medicine. The screening process takes 496 active ingredients of traditional Chinese medicine with high-quality transcriptome response data as the initial candidate library, and gradually enriches candidate molecules that simultaneously possess targeted action, biological rationality and potential for drug development through multiple rounds of constraint conditions.

At the functional level, the RGES score was first adopted to quantitatively evaluate the overall reversal ability of small molecules against the abnormal co-expression characteristics of IPF - aging. The more negative the RGES value is, the stronger the correction effect of this molecule on the abnormal expression pattern of the disease at the transcriptome level. Secondly, at the Network level, the topological distance between the set of small molecule targets of traditional Chinese medicine and the aging-

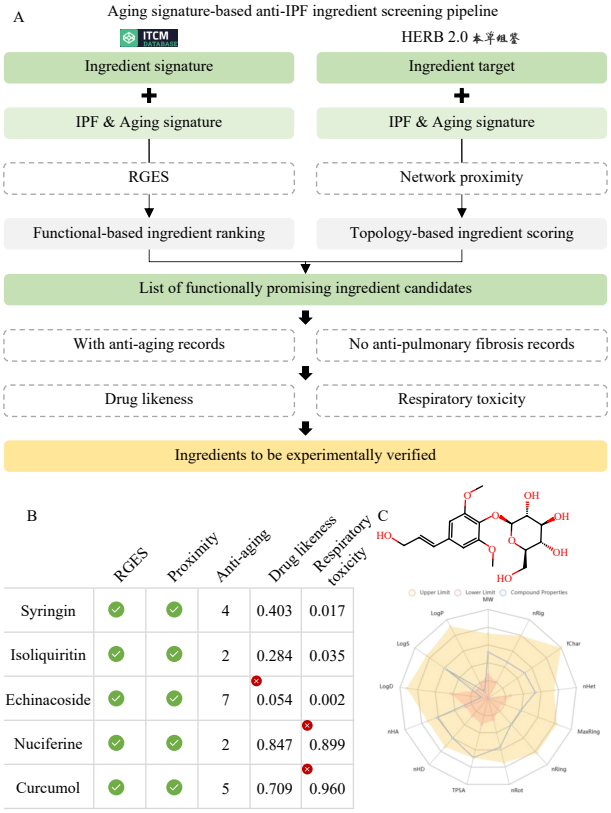


Fig. 4 Multidimensional screening for identifying candidate traditional chinese medicine small molecules with synergistic effects against IPF and senescence. (A) Multidimensional screening workflow for identifying anti-IPF and anti-senescence TCM small molecules; (B) Comparison of core screening parameters for the top 5 candidate small molecules; (C) Chemical structure and key physicochemical parameters of syringin.

IPF functional module in the protein interaction network is calculated based on the Network Proximity algorithm. Among them, the lower the *Z*-score, the closer the functional correlation between the target and the core pathway of the disease, and the clearer the potential targeting effect. At the biological and translational level, the previous research evidence of each candidate component in the fields of anti-aging (including studies related to senescence, SASP, aging, and senolytic) and anti-pulmonary fibrosis was further systematically retrieved through the PubMed database. To comprehensively assess its research foundation and potential innovative value. Finally, at the level of drug development feasibility, the drug potential of small molecules was evaluated using the quantitative estimate of drug-likeness QED scoring system, combined with the respiratory toxicity prediction model of ADMETlab 2.0 Conduct a prospective assessment of the potential medication risks of candidate molecules. Based on the screening results from the above four dimensions (Fig. 4B), ultimately, five small molecules of traditional Chinese medicine demonstrated outstanding potential in the synergistic intervention of anti-IPF and aging. Among them, Syringin demonstrated the best or near-best comprehensive performance in all core evaluation indicators, thus standing out significantly among the candidate molecules (Fig. 4C).

In terms of the ability to reverse disease characteristics, the RGES value of syringin for the IPF-aging co-expression feature is −0.6269, suggesting that it has a significant ability to reverse abnormal expression patterns at the transcriptome level. At the disease network level, the *Z*-scores of its network proximity in the AF-senescence and IPF-senescence functional modules were −1.2359 and −0.5698 respectively, indicating that there is a high degree of topological proximity and functional correlation between its target sites and the core functional modules of the

disease. Support it as it may function by directly intervening in the key senescent-fibrotic pathway. In terms of research innovation, systematic literature search results show that syringin has been reported to have clear biological activities related to anti-aging, but no studies have applied it in the intervention of pulmonary fibrosis or the treatment of IPF, suggesting that it has significant space for innovative exploration and potential translational value in this disease field. In terms of the potential and safety of the drug, the *QED* value of syringin is 0.403, showing a moderate but acceptable drug-like characteristic. Meanwhile, its respiratory toxicity prediction score is only 0.017, suggesting that it has a relatively low toxicity risk in the context of respiratory system medication.

Based on the above multi-dimensional and systematic comprehensive assessment, syringin was identified as the most promising candidate small molecule of traditional Chinese medicine for anti-IPF in this study and was further incorporated into the subsequent *in vivo* and *in vitro* experimental verification and mechanism of action analysis system.

3.5. Syringin improves BLM-induced pulmonary fibrosis in mice

To evaluate the anti-fibrotic effect of syringin, we first examined its function in an animal model of pulmonary fibrosis. The bleomycin-induced pulmonary fibrosis mouse model is the most recognized and widely used animal model in pulmonary fibrosis research [30]. Therefore, we constructed a bleomycin-induced mouse pulmonary fibrosis model using a single airway injection of bleomycin-to test the therapeutic potential of syringin. After the animals in each group were treated with BLM or normal saline on day 0, they were given SG or normal saline by gavage starting from day 1 for 21 d (Fig. 5A).

During the entire experimental period (0–21 days), the survival rate of mice in the BLM treatment group was significantly lower than that in the control group, while the survival rate of the SG group was higher than that of the BLM group (Fig. 5B). Meanwhile, the use of SG also mitigated the weight loss in mice induced by BLM to a certain extent (Fig. 5C). Hydroxyproline is a non-essential amino acid present in collagen and other extracellular animal proteins. It plays a key role in the synthesis of collagen and the thermodynamic stability of the triple helix conformation of collagen and related tissues. Therefore, the content of HYP is a key indicator reflecting the degree of collagen deposition in lung tissue [31]. The HYP content in the lung tissue of mice in the BLM group was significantly higher than that in the control group. Compared with the BLM group, the HYP content in the SG group was significantly decreased, indicating that the drug effectively reduced lung collagen deposition (Fig. 5D).

To further explore the therapeutic effect of SG, histopathological analysis was conducted on lung tissue. HE staining (Fig. 5E) showed that the alveolar structure of mice in the normal control group was intact, the alveolar walls were relatively thin, the alveolar epithelium was well preserved, and there was no obvious infiltration of inflammatory cells. In the BLM group, the alveolar structure was severely damaged, the alveolar walls were significantly thickened, a large amount of interstitial fibrous tissue accumulated, and fibrotic foci were widely fused. In the SG treatment group, the alveolar septum remained thickened, but the fibrotic lesion was more localized and had a smaller range. The quantitative assessment of PF severity using the Ashcroft score based on HE-stained pathological images (Fig. 5F) showed that the score of the SG treatment group was significantly lower than that of the BLM group. Masson tricolor staining showed that the alveolar septum of mice in the BLM group was significantly thickened and filled with a large amount of blue-stained collagen fibers. Compared with the BLM group, the low-staining blue areas in the SG treatment group were significantly reduced (Fig. 5G). The result was quantified by collagen volume fraction analysis (Fig. 5H).

The immunohistochemical staining results of α-SMA, COL-I, and TGF-β1 proteins were similar (Fig. 5I), all showing that SG treatment reduced BLM-induced lung tissue structure damage and collagen deposition in mice. In addition, Western blotting analysis revealed that the protein expression levels of COL-I, COL-III and α-SMA in the lung tissue of the SG treatment group were significantly lower than those of the bleomycin group (Figs. 5J and 5K), indicating that SG treatment could inhibit the activation of myofibroblasts and the synthesis of extracellular matrix (ECM). These results all confirmed the anti-fibrotic effect of SG in the mouse model of pulmonary fibrosis.

3.6. Syringin inhibits TGF-β -induced proliferation and activation of NIH/3T3 cells and alleviates pulmonary fibrosis

To evaluate the effect of SG on fibroblast function, we first conducted *in vitro* experiments using NIH/3T3 fibroblasts. We evaluated the effect of SG on fibroblast activity by using the CCK-8 method. The results showed that SG had no significant inhibitory effect on fibroblast activity within the range of 0−100 μmol·L^{-1}, indicating that the drug toxicity was relatively low at this concentration (Fig. 6A). Therefore, 10, 20 and 40 μmol·L^{-1} were selected for subsequent experiments. Then, fibroblasts were stimulated with TGF-β to induce their differentiation into myofibroblasts, thereby simulating the PF microenvironment.

As shown in the figure (Fig. 6B)， SG significantly inhibited TGF-β-induced cell proliferation in a dose-dependent and time-dependent manner. High-dose SG (40 μmol·L^{-1}) significantly inhibited TGF-β-induced fibroblast proliferation, and the effect was more obvious compared with the medium and low-dose groups. On this basis, a concentration of 40 μmol·L^{-1} was selected for the subsequent experiments. The effect of SG on the migration ability of fibroblasts was evaluated through wound healing experiments. Compared with the simple TGF-β treatment group, the SG treatment group significantly slowed down the cell migration rate within 24 h, resulting in a significant reduction in the wound healing area (Figs. 6C and 6D), confirming that SG can effectively inhibit the migration of fibroblasts.

To further confirm whether SG can inhibit abnormal collagen deposition in the extracellular matrix, we detected the expression levels of Col-I, Col-III, α-SMA, FN and Vim. The Western blotting results (Figs. 6E and 6F) showed that TGF-β stimulation significantly increased the expressions of COL-I, COL-III, α-SMA, FN and Vim, while SG treatment significantly decreased the levels of these proteins. These findings suggest that SG effectively hinders fibroblast activation and the synthesis of ECM elements. This was corroborated in subsequent RT-qPCR and immunofluorescence analyses (Figs. 6G, 6H, and 6I). In summary, our experimental data illustrate that SG can effectively suppress the growth and movement of lung fibroblasts, as well as the augmentation of their capacity to generate extracellular matrix prompted by TGF-β.

3.7. Syringin exerts anti-aging effects by inhibiting the ATR/CHK1 signaling pathway in NIH/3T3 cells

Based on the conclusion revealed by the previous multi-omics integration analysis that the excessive activation of the fibroblast senescence program is one of the core pathological events of IPF, this study further systematically analyzed the molecular mechanism by which syringin exerts anti-aging effects in the cell model. The focus is on the signaling pathways related to DNA damage response (DDR).

RNA-seq analysis was performed on TGF-β-stimulated NIH/3T3 fibroblasts (Fig. 7A), and the results showed that, compared with the control group, The “ATR in response to replication stress” pathway was significantly activated in the TGF-β treatment group

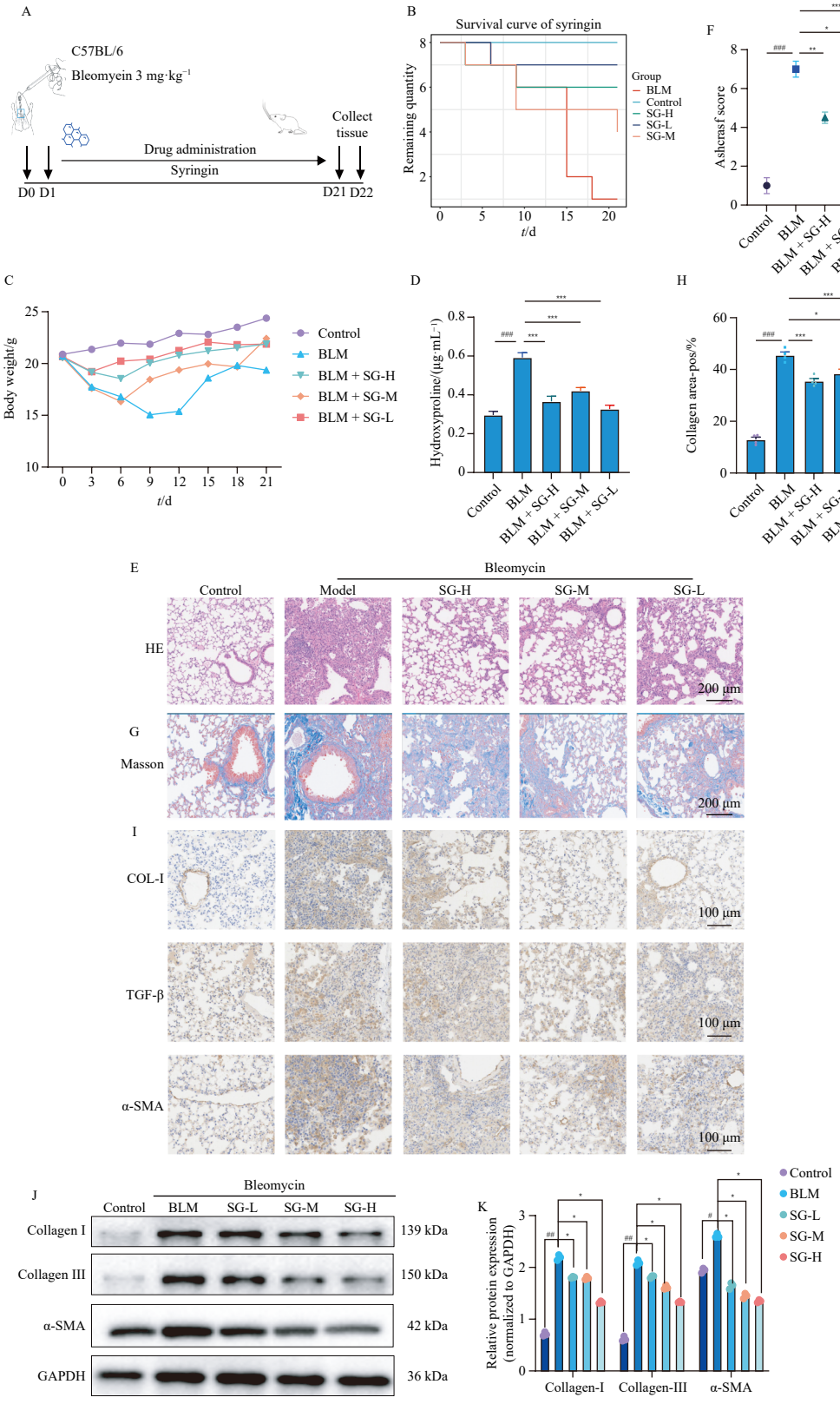


Fig. 5 Syringin improves BLM-induced pulmonary fibrosis in mice. (A) Establishment of the BLM animal model and dosing regimen (n = 8). (B, C) Survival and body weight trends in mice from days 0 to 21 (n = 8). (D) Hypoxanthine (HYP) content in mouse lung tissue. (E) Hematoxylin and eosin (HE) staining of lung tissue. (F) Ashcroft score of lung tissue, where 0 indicates no fibrosis and scores from 1 to 8 represent progressively increased fibrosis severity. (G) Masson trichrome staining of lung tissue. (H) Analysis of collagen volume fraction by Masson trichrome staining. (I) Western blot results for Collagen I, Collagen III, and α-SMA protein expression in each group. (J) Collagen I, Collagen III, and α-SMA protein levels normalized to GAPDH in each group. (K) Representative immunohistochemical images of Col1a1, TGF-β, and α-SMA in lung tissue. Results represent mean ± SD, n = 3. $^{\#}P < 0.05$, $^{\#\#}P < 0.01$, $^{\#\#\#}P < 0.001$ *vs* control group; $^{*}P < 0.05$, $^{**}P < 0.01$, $^{***}P < 0.001$ *vs* BLM group.

(Fig. 7B), suggesting that replication stress-related DDR signaling plays an important role in fibroblast senescence and fibrotic activation. It is worth noting that the intervention of syringin can significantly reverse the activation trend of the above pathway (Fig. 7C), indicating that this compound may alleviate replication stress and DNA damage accumulation by regulating the ATR/CHK1 axis. The ATR/CHK1 signaling pathway is the core regulatory axis for cells to respond to replication stress states

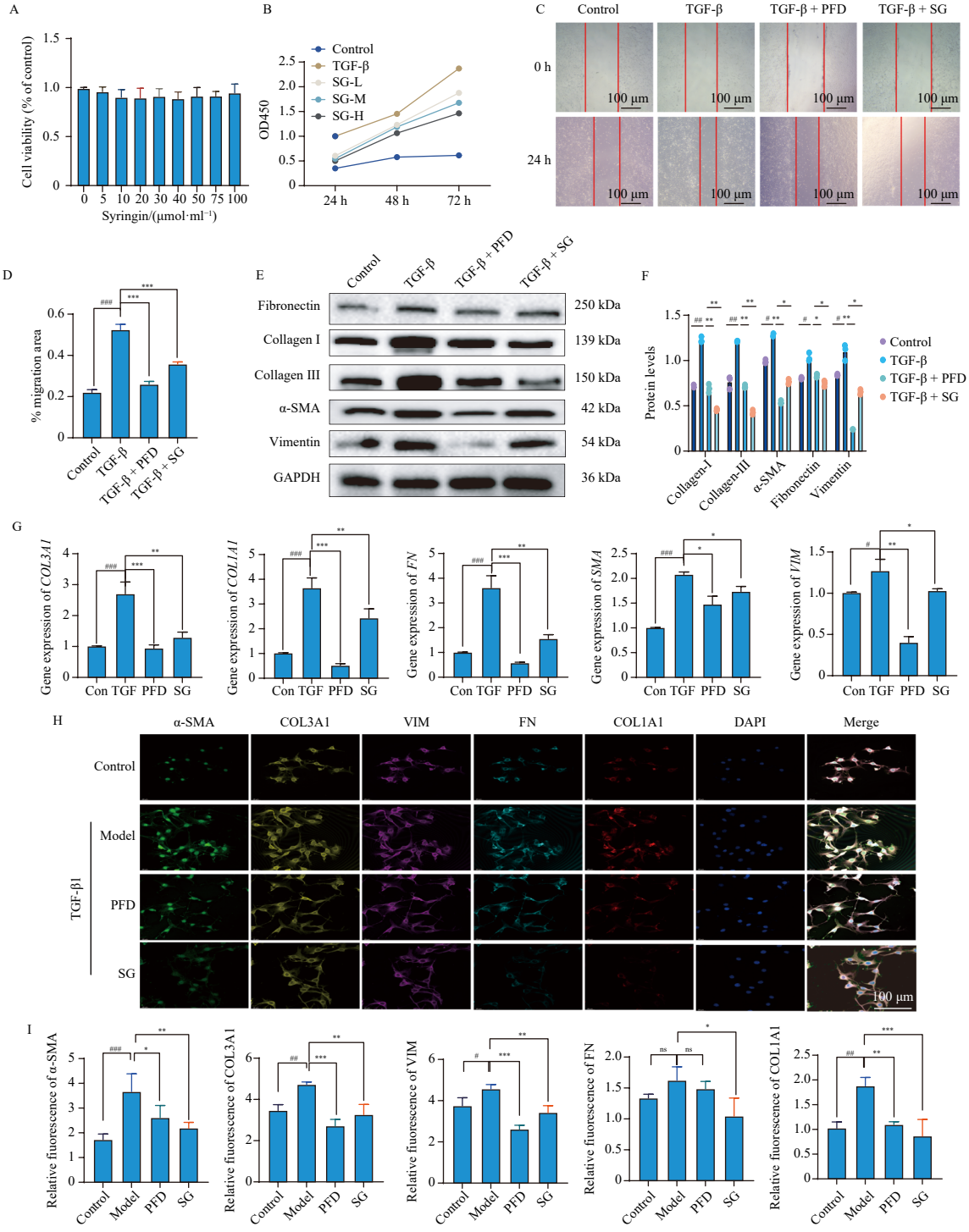


Fig. 6 Syringin inhibits TGF-β-induced proliferation and activation of NIH/3T3 cells and alleviates pulmonary fibrosis. (A) Dose-dependent effects of SG on cell viability. (B) SG inhibits TGF-β-induced cell proliferation over time: Fibroblasts treated with SG alone or in combination with different concentrations of SG; 10 μmol·mL^{-1} (L), 20 μmol·mL^{-1} (M), 40 μmol·mL^{-1} (H). (C) Wound healing assay demonstrating SG inhibition of cell migration. (D) Quantification of migrated cell area. (E) Western blot results showing protein expression of Fibronectin, Collagen I, Collagen III, α-SMA, and Vimentin in each group. (F) Fibronectin, Collagen I, Collagen III, α-SMA, and Vimentin protein levels normalized to GAPDH in each group. (G) RT-qPCR results for Fibronectin, Collagen I, Collagen III, α-SMA, and Vimentin in each group. (H) Immunofluorescence results for Fibronectin, Collagen I, Collagen III, α-SMA, and Vimentin in each group. (I) Quantification of immunofluorescence results for Fibronectin, Collagen I, Collagen III, α-SMA, and Vimentin in each group. Results represent mean ± SD, $n = 3$. $^{\#}P < 0.05$, $^{\#\#}P < 0.01$, $^{\#\#\#}P < 0.001$ *vs* control group; $^{*}P < 0.05$, $^{**}P < 0.01$, $^{***}P < 0.001$ *vs* TGF-β group.

such as slowed, paused or broken replication forks during DNA replication. Its continuous activation can induce irreversible cellular senescence phenotypes through the downstream p53-P21-P16 cell cycle inhibition pathway. Therefore, this signaling axis is regarded as an important molecular hub connecting DNA damage, cellular senescence and the progression of fibrosis.

We first examined the effect of SG on fibroblast senescence. An oxidative stress-related cellular senescence model was constructed by inducing NIH/3T3 cells with BLM. The SA-β-GAL staining results showed that BLM treatment significantly increased the proportion of senescent fibroblasts, while syringin intervention significantly inhibited this effect, suggesting that it effectively inhibited the formation of senescent phenotypes (Fig. 7D). Subsequently, we further detected the mRNA expression levels of SASP factors by RT-qPCR. The results showed (Fig. 7E) that BLM induction significantly upregulated the expression

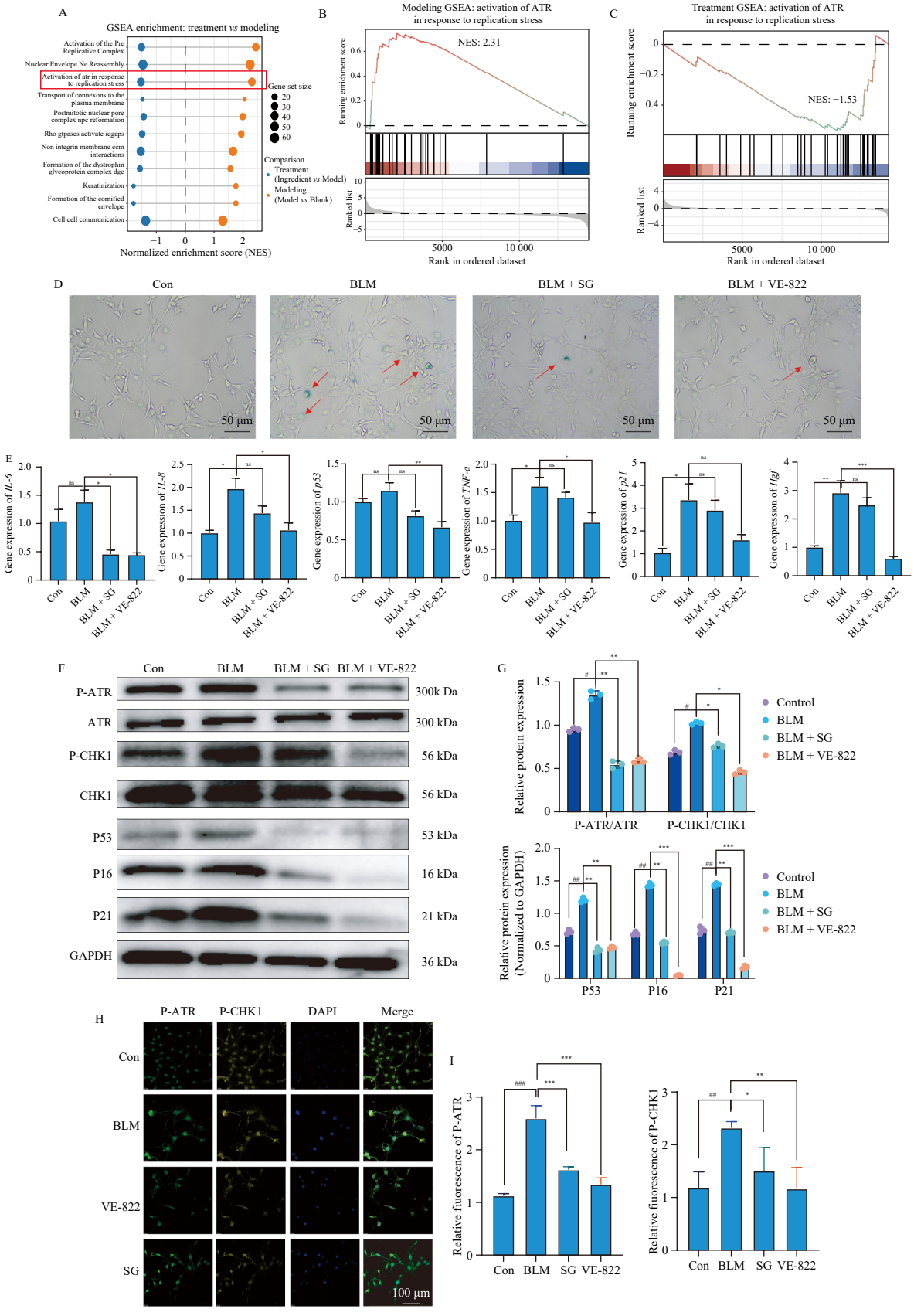


Fig. 7 Syringin exerts anti-aging effects by inhibiting the ATR/CHK1 signaling pathway in NIH/3T3 cells. (A) IPF-aging-associated Reactome pathways significantly reversed by syringin intervention (modeling *vs* drug administration). (B) Activation of the ATR replication stress pathway after BLM induction (model group *vs* control group, GSEA analysis). (C) Suppression of the ATR replication stress pathway after syringin intervention (drug administration group *vs* model group, GSEA analysis). (D) SA-β-gal staining results in each group. (E) RT-qPCR results for SASP in each group. (F) Western blot results for P-ATR, ATR, P-CHK1, CHK1, p53, p21, and p16 protein expression in each group. (G) Quantitative analysis of P-ATR/ATR and P-CHK1/CHK1 ratios, with p53, p21, and p16 normalized to GAPDH values. (H) Immunofluorescence results for P-ATR and P-CHK1 in each group. (I) Quantification of immunofluorescence results for P-ATR and P-CHK1 in each group. Results represent mean ± SD, $n = 3$. $^{\#}P < 0.05$, $^{\#\#}P < 0.01$, $^{\#\#\#}P < 0.001$ *vs* control group; $^{*}P < 0.05$, $^{**}P < 0.01$, $^{***}P < 0.001$ *vs* BLM group.

of various inflammatory factors and chemokines in fibroblasts, while syringin treatment significantly downregulated the transcriptional levels of these SASP factors, suggesting that SG can alleviate the pro-inflammatory microenvironment effect mediated by senescent fibroblasts.

To further verify whether syringin alleviates fibroblast senescence by inhibiting the ATR/CHK1 pathway, we introduced the ATR/CHK1-specific inhibitor VE-822 as a pathway intervention control. The Western blot results showed that compared with the control group, BLM treatment significantly enhanced the phosphorylation levels of ATR and CHK1, accompanied by a marked upregulation of the protein expressions of aging markers p53, p21 and p16, suggesting that the DDR checkpoint was strongly activated. After the intervention with syringin, the above ratios and the expression levels of p53, p21 and p16 all showed a significant and dose-dependent downward trend, and the effect was highly consistent with that of the VE-822 treatment group, indicating that SG could effectively inhibit the ATR/ CHK1-mediated senescence signal cascade (Figs. 7F and7G, Supplementary Figure S1). To further analyze the activation status and subcellular localization changes of ATR/CHK1, immunofluorescence staining analysis was conducted on P-ATR and P-CHK1 in this study. The results showed that the fluorescence signals of P-ATR and P-CHK1 in the BLM treatment group were significantly enhanced and mainly located in the nucleus, suggesting that the DNA damage checkpoint was activated and involved in nuclear signal transduction. However, the treatment with syringin significantly reduced the fluorescence intensity and nuclear aggregation degree of the above kinases. It is suggested that SG can suppress the abnormal activation state of ATR/CHK1 from both spatial and signal strength aspects (Figs. 7H and7I).

3.8. Syringin inhibits downstream signaling through CHK1-dependent mechanisms

To investigate the potential interaction between syringin and key targets of the ATR/CHK1 pathway, molecular docking simulations of syringin with CHK1 and ATR were performed in this study, combined with pathway inhibition experiments to further validate its target-binding potential. The results showed that the predicted binding affinities of syringin for CHK1 and ATR were −7.4 and −7.0 kcal·mol^{-1}, respectively, suggesting that this compound may interact with both kinases.

In the CHK1 docking model (Figs. 8A, 8B and 8C), syringin was localized within the catalytic pocket and formed multiple predicted hydrogen bonds with surrounding residues, including Asn59, Cys87, Glu91, Asp148, and Phe149 (Supplementary Table S1). Additionally, hydrophobic contacts involving Leu84 were observed, which may contribute to ligand stabilization within the binding cavity. In contrast, fewer stable interactions were predicted in the ATR docking model, where syringin formed hydrogen bonds with Asp2335, Val2380, Asn2480, and Asn2496, along with hydrophobic contacts involving Ile2377, Val2493, and Asp2494. Molecular docking analysis indicated that syringin could accommodate the binding pockets of both CHK1 and ATR. The slightly lower predicted binding energy and more extensive hydrogen bond network in the CHK1 complex suggested a certain degree of structural preference of syringin for CHK1. These computational observations provide preliminary structural insights for subsequent experimental validation.

To further assess whether syringin interacts with CHK1 in intact cells, a CETSA was employed. NIH/3T3 cells were treated with syringin or the control compound DMOG for 2 h, followed by gradient heating from 35 to 70 °C. The results showed that compared with the DMOG control group, syringin treatment induced a rightward shift in the thermal melting curve of CHK1, whereas DMOG did not exhibit a thermal stabilization effect on CHK1

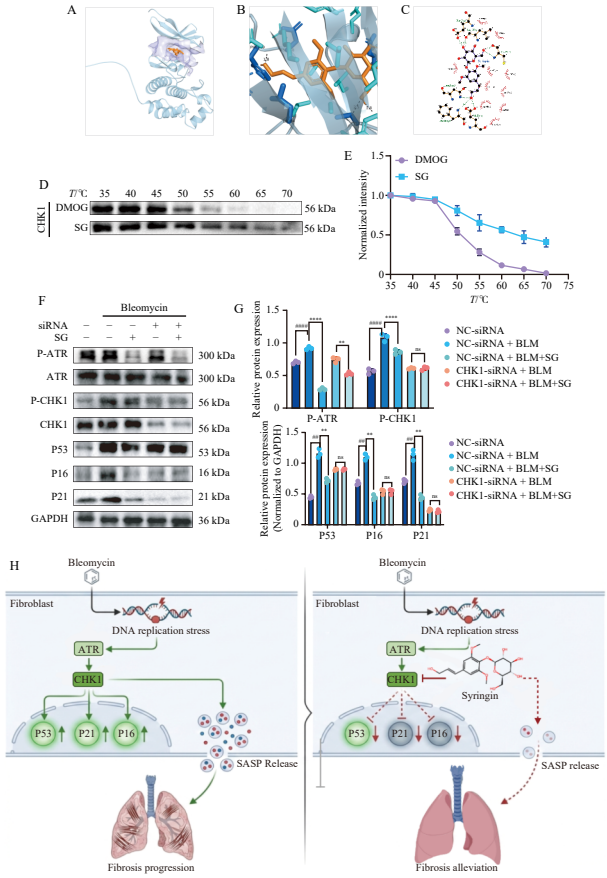


Fig. 8 Syringin inhibits downstream signaling through CHK1-dependent mechanisms. (A) Overall binding mode of syringin (orange) within the CHK1 binding pocket (purple surface). (B) Three-dimensional interaction details between syringin and key residues in the CHK1 binding pocket. (C) Two-dimensional interaction diagram illustrating hydrogen bonds and hydrophobic interactions between syringin and CHK1. (D) Western blot analysis of CHK1 protein stability after treatment with syringin or DMOG. (E) Quantitative analysis of CHK1 thermal melting curves derived from the cellular thermal shift assay (CETSA). CHK1 protein levels were normalized to the signal at 35 °C. (F) Western blot analysis of P-ATR, ATR, P-CHK1, CHK1, p53, p21, and p16 protein expression in each experimental group. (G) Quantitative analysis of P-ATR/ATR and P-CHK1/CHK1 ratios, while p53, p21, and p16 expression levels were normalized to GAPDH. (H) Schematic illustration of the proposed ATR-CHK1-p53 signaling pathway involved in the anti-fibrotic and anti-senescent effects of syringin. Results represent mean ± SD, $n = 3$. $^{\#}P < 0.05$, $^{\#\#}P < 0.01$, $^{\#\#\#}P < 0.001$ *vs* control group. $^{*}P < 0.05$, $^{**}P < 0.01$, $^{***}P < 0.001$ *vs* BLM group.

(Figs. 8D and 8E). These findings indicate that syringin may interact with CHK1 and increase its thermal stability in cells.

To determine whether CHK1 is required for the regulatory effects of syringin, transient knockdown of CHK1 was performed in NIH/3T3 cells using siRNA. Western blotting analysis confirmed that siRNA treatment significantly reduced CHK1 protein expression, indicating effective knockdown. In control cells, syringin treatment significantly decreasedthe protein expression levels of p-CHK1, P53, P21, and P16, indicating inhibition of CHK1-related senescence signaling. However, in CHK1-knockdown cells, syringin treatment no longer produced significant changes in the expression of these proteins (Figs. 8F and 8G). These results indicate that the regulatory effects of syringin on downstream signaling are at least partially mediated by CHK1-dependent signaling.

In summary, this study provides multi-level evidence, including transcriptomic analysis, protein expression profiling, molecular docking, CETSA, and functional knockdown experiments, supporting CHK1 as a potential molecular target of syringin. Through modulation of the ATR-CHK1-p53 signaling pathway, syringin suppresses the activation of downstream senescence-associated regulators, including p53, p21, and p16, reduces the proportion of SA-β-gal–positive cells and the secretion of SASP factors, and

ultimately attenuates fibroblast senescence and the pro-fibrotic microenvironment. These findings provide mechanistic insight into the anti-fibrotic effects of syringin (Fig. 8H).

4. Discussion

Through systematic integration of multi-cohort bulk RNA-seq, scRNA-seq, and *in vivo*/*in vitro* functional experiments, this study reveals a significant and consistently upregulated aberrant activation of the pulmonary senescence program in idiopathic pulmonary fibrosis (IPF). The study findings indicate that IPF exhibits a significant enrichment of molecular traits within the fundamental gene modules associated with aging, which are elevated as individuals age. Conversely, the aging-related suppression process does not exhibit a comparable hindrance in IPF. This implies that IPF does not merely represent an uncomplicated form of "accelerated aging", but rather a targeted enhancement of distinct pathological pathways within the aging process. At the cellular level, fibroblasts have been identified as the core cell type that carries the abnormal activation of the senescence process. Further screening and verification based on the framework of systems biology revealed that the small molecule of traditional Chinese medicine, syringin can significantly alleviate fibroblast senescence and its pro-fibrotic phenotype, at least in part through modulation of the ATR/CHK1–p53 signaling axis. These findings collectively construct a systematic molecular picture of "aging-driven fibrosis".

IPF is widely recognized as a strong age-related disease [32], but for a long time, aging has been more regarded as a background risk factor or concomitant phenomenon of IPF rather than a direct pathological driving force [33]. Previous studies have mostly focused on individual aging markers (such as p16, SA-β-GAL) or specific cell types [34, 35], lacking system-level evidence to clarify the overall relationship between the aging process and the molecular phenotype of IPF. In this study, by directly integrating and comparing the age gradient characteristics of lung tissue constructed by GTEx with the transcriptome of multiple cohorts of IPF, it was systematically demonstrated at the human lung tissue level that there is a highly consistent enrichment relationship between the differential expression profile of IPF and age-upregulated aging genes. This discovery holds significant theoretical importance. It indicates that IPF does not simply replicate the entire molecular trajectory of normal aging, but pathologically amplifies the modules related to inflammation, extracellular matrix remodeling and stress response in the aging program, while lacking corresponding inhibition of some downregulated aging programs. This "modular selective activation" model suggests that aging is not a homogeneous process, and the fate of its different branches in diseases depends on the tissue environment and the background of chronic damage. IPF precisely drives the continuous progression of diseases by hijacking the pro-fibrotic dimension in the aging process.

The DNA damage response (DDR) pathway, especially the ATR/CHK1 signaling axis, is generally regarded as a protective mechanism for maintaining genomic stability and cell survival [36]. Under acute injury or replication stress, the activation of this pathway helps cells repair damage and resume proliferation [37]. However, the results of this study indicate that in the context of chronic stress related to IPF, the continuous activation of the ATR/CHK1 pathway may lead to pathological functional transformation. In the fibroblast senescence model, we observed that the activation of ATR/CHK1 was accompanied by the continuous upregulation of the p53-P21-P16 axis and the stable maintenance of the SASP phenotype. This suggests that ATR/CHK1 is no longer merely a transient stress response, but has become a key node in maintaining the aging state and the pro-fibrotic microenvironment. This phenomenon supports the "context-dependent signal transformation" theory, that is, in chronic diseases, signal pathways that should have protective effects may transform into pathological drivers due to continuous activation. This mechanism provides a new molecular explanation for understanding the irreversibility of aging in IPF.

In recent years, intervention strategies targeting aging have gradually attracted attention in IPF research. Senolytic drugs (such as the combination of dasatinib and quercetin) have been proven to improve certain fibrosis indicators in animal models and early clinical studies [38]. However, such strategies work by directly eliminating senescent cells, which may be accompanied by cell loss and potential toxicity risks. Their long-term safety and applicable population remain controversial [39, 40]. In contrast, the syringin proposed and verified in this study is a typical senomorphic regulatory strategy. By inhibiting the aging maintenance pathway rather than directly eliminating cells, it may have potential advantages in terms of safety and tissue homeostasis maintenance. In addition, the currently used anti-fibrotic drugs in clinical practice (such as pirfenidone and nintedanib) mainly target downstream fibrotic pathways [41], which have a certain delaying effect on disease progression, but they cannot reverse the established pathological state. This study starts from the more upstream pathological process of aging, providing a new perspective for explaining the limited efficacy of existing treatment methods and laying a theoretical foundation for the design of combined intervention strategies.

Although this study has revealed a key mechanism by which syringin exerts anti-fibrotic and anti-aging effects, closely associated with inhibition of the ATR/CHK1 signaling pathway through multi-level data integration and experimental validation, several limitations still exist. First, regarding the mechanistic investigation, although we have confirmed that the anti-aging effect of syringin is dependent on CHK1 through CHK1 knockdown experiments, and verified its direct binding to CHK1 by molecular docking and CETSA, the potential contribution of additional targets or parallel pathways cannot be excluded. Moreover, the dose–effect relationship between syringin and components of the ATR/CHK1 pathway has not been systematically elucidated. The concentration of syringin used in this study was primarily determined based on preliminary cytotoxicity assays and pharmacodynamic activity screening. Future studies are needed to conduct more comprehensive dose-gradient experiments to clarify its concentration-effect relationship and therapeutic window. Second, regarding the *in vivo* efficacy evaluation, although we have employed gold-standard indicators such as hydroxyproline content and Ashcroft score to comprehensively evaluate the anti-fibrotic efficacy of syringin, the current study still relies mainly on endpoint-based histological and biochemical analyses, lacking real-time monitoring of the dynamic progression of fibrosis. Future research may introduce advanced imaging techniques such as small-animal *in vivo* micro-computed tomography (micro-CT) to longitudinally track structural changes in the lung, thereby more intuitively and dynamically evaluating the intervention effect of syringin on fibrosis progression. Furthermore, this study is primarily based on the bleomycin-induced acute pulmonary fibrosis model, which still has limitations in simulating the chronic progressive course and spatial heterogeneity of human IPF. Meanwhile, the safety of long-term inhibition of the DDR pathway in the treatment of chronic diseases still needs to be evaluated through more systematic animal experiments and preclinical studies. These limitations will be progressively addressed in our future research.

This study not only reveals the systematic activation of the aging program in IPF and its key regulatory nodes, but also proposes a scalable multi-dimensional screening framework for small molecules in traditional Chinese medicine, providing a new methodological paradigm for drug discovery of senecsence-re-

lated diseases. Syringin, as a natural small molecule with definite anti-aging activity and good safety, provides a strong candidate for the development of new anti-IPF treatment strategies.

5. Conclusion

This work delineates the multicellular landscape and molecular wiring of senescence in IPF and establishes a robust integrative strategy to identify anti-senescence therapeutics. We demonstrate that syringin is a potent modulator of the ATR/CHK1–p53 axis with dual anti-senescence and anti-fibrotic activity, highlighting a mechanistically grounded and actionable strategy for next-generation IPF therapy.

Funding

This work was supported by the National Natural Science Foundation of China (No. 82170074), the China Postdoctoral Science Foundation (No. 2025M773940), Ningbo Clinical Research Center for Res piratory Disease (No. 2022L004), Ningbo Natural Science Foundation (No. 2022J241), Zhejiang Provincial Nature Science Foundation of China (No. LY24H010002), Ningbo Health Branding Subject Fund (No. PPXK2018-05) , the Talent Introduction Project of Yongjiang River (No. 2021B-016-G), and Ningbo Natural Science Foundation (No.2023J318).

Supplementary data

Data will be available on request by sending E-mail to the corresponding authors.

Declaration of competing interest

The authors declare that they have no known competing financial interests or personal relationships that could have appeared to influence the work reported in this paper.

References

1 Moss BJ, Ryter SW, Rosas IO. Pathogenic mechanisms underlying idiopathic pulmonary fibrosis. *Annu Rev Pathol*. 2022;17:515-546. https://doi.org/10.1146/annurev-pathol-042320-030240.
2 Liu GY, Budinger GRS, Dematte JE. Advances in the management of idiopathic pulmonary fibrosis and progressive pulmonary fibrosis. *BMJ*. 2022;377:e066354. https://doi.org/10.1136/bmj-2021-066354.
3 Karampitsakos T, Juan-Guardela BM, Tzouvelekis A, et al. Precision medicine advances in idiopathic pulmonary fibrosis. *EBioMedicine*. 2023;95:104766. https://doi.org/10.1016/j.ebiom.2023.104766.
4 Cho SJ, Stout-Delgado HW. Aging and lung disease. *Annu Rev Physiol*. 2020;82:433-459. https://doi.org/10.1146/annurev-physiol-021119-034610.
5 Alder JK, Armanios M. Telomere-mediated lung disease. *Physiol Rev*. 2022;102(4):1703-1720. https://doi.org/10.1152/physrev.00046.2021.
6 Schuliga M, Pechkovsky DV, Read J, et al. Mitochondrial dysfunction contributes to the senescent phenotype of IPF lung fibroblasts. *J Cell Mol Med*. 2018;22(12):5847-5861. https://doi.org/10.1111/jcmm.13855.
7 Schafer MJ, White TA, Iijima K, et al. Cellular senescence mediates fibrotic pulmonary disease. *Nat Commun*. 2017;8:14532. https://doi.org/10.1038/ncomms14532.
8 Huang J, Gacha-Garay MJ, Wang Y, et al. Alternative polyadenylation contributes to fibroblast senescence in pulmonary fibrosis. *Aging Cell*. 2025;24(10):e70179. https://doi.org/10.1111/acel.70179.
9 Liang J, Liu N, Liu X, et al. Mitogen-activated protein kinase-activated protein kinase 2 inhibition attenuates fibroblast invasion and severe lung fibrosis. *Am J Respir Cell Mol Biol*. 2019;60(1):41-48. https://doi.org/10.1165/rcmb.2018-0033OC.
10 Guan RJ, Yuan L, Li JP, et al. Bone morphogenetic protein 4 inhibits pulmonary fibrosis by modulating cellular senescence and mitophagy in lung fibroblasts. *Eur Respir J*. 2022;60(6):2102307. https://doi.org/10.1183/13993003.02307-2021.
11 Schuliga M, Read J, Blokland KEC, et al. Self DNA perpetuates IPF lung fibroblast senescence in a cGAS-dependent manner. *Clin Sci (Lond)*. 2020;134(7):889-905. https://doi.org/10.1042/CS20191160.
12 GTEx Consortium. The Genotype-Tissue Expression (GTEx) project. *Nat Genet*. 2013;45(6):580-585. https://doi.org/10.1038/ng.2653.
13 Zhai ZY, Lin ZW, Meng XH, et al. DiSignAtlas: an atlas of human and mouse disease signatures based on bulk and single-cell transcriptomics. *Nucleic Acids Res*. 2024;52(D1):D1236-D1245. https://doi.org/10.1093/nar/gkad961.
14 Barrett T, Wilhite SE, Ledoux P, et al. NCBI GEO: archive for functional genomics data sets--update. *Nucleic Acids Res*. 2013;41:D991-D995. https://doi.org/10.1093/nar/gks1193.
15 Wolock SL, Lopez R, Klein AM. Scrublet: computational identification of cell doublets in single-cell transcriptomic data. *Cell Systems*. 2019;8(4):281-291.e9. https://doi.org/10.1016/j.cels.2018.11.005.
16 Wang B, Wei W, Long SR, et al. CENPA acts as a prognostic factor that relates to immune infiltrates in gliomas. *Front Neurol*. 2022;13:1015221. https://doi.org/10.3389/fneur.2022.1015221.
17 Xu SB, Hu EQ, Cai YT, et al. Using clusterProfiler to characterize multiomics data. *Nat Protoc*. 2024;19(11):3292-3320. https://doi.org/10.1038/s41596-024-01020-z.
18 Wang QN, Lin YS, Yu WG, et al. The core role of macrophages in hepatocellular carcinoma: the definition of molecular subtypes and the prognostic risk system. *Front Pharmacol*. 2023;14:1228052. https://doi.org/10.3389/fphar.2023.1228052.
19 Tian SS, Zhang JB, Yuan SL, et al. Exploring pharmacological active ingredients of traditional Chinese medicine by pharmacotranscriptomic map in ITCM. *Brief Bioinform*. 2023;24(2):bbad027. https://doi.org/10.1093/bib/bbad027.
20 Gao K, Liu L, Lei S, et al. HERB 2.0: an updated database integrating clinical and experimental evidence for traditional Chinese medicine. *Nucleic Acids Res*. 2025;53(D1):D1404-D1414. https://doi.org/10.1093/nar/gkae1037.
21 Samart K, Tuyishime P, Krishnan A, et al. Reconciling multiple connectivity scores for drug repurposing. *Brief Bioinform*. 2021;22(6):bbab161. https://doi.org/10.1093/bib/bbab161.
22 Guney E, Menche J, Vidal M, et al. Network-based in silico drug efficacy screening. *Nat Commun*. 2016;7:10331. https://doi.org/10.1038/ncomms10331.
23 Cook HV, Doncheva NT, Szklarczyk D, et al. Viruses.STRING: a virus-host protein-protein interaction database. *Viruses*. 2018;10(10):1-11. doi:10.3390/v10100519.
24 Xiong GL, Wu ZX, Yi JC, et al. ADMETlab 2.0: an integrated online platform for accurate and comprehensive predictions of ADMET properties. *Nucleic Acids Res*. 2021;49(W1):W5-W14. https://doi.org/10.1093/nar/gkab255.
25 Tashiro J, Rubio GA, Limper AH, et al. Exploring animal models that resemble idiopathic pulmonary fibrosis. *Front Med (Lausanne)*. 2017;4:118. https://doi.org/10.3389/fmed.2017.00118.
26 Berman HM, Westbrook J, Feng Z, et al. The protein data bank. *Nucleic Acids Res*. 2000;28(1):235-242. https://doi.org/10.1093/nar/28.1.235.
27 Morris GM, Huey R, Lindstrom W, et al. AutoDock4 and AutoDockTools4: automated docking with selective receptor flexibility. *J Comput Chem*. 2009;30(16):2785-2791. https://doi.org/10.1002/jcc.21256.
28 Trott O, Olson AJ. AutoDock Vina: improving the speed and accuracy of docking with a new scoring function, efficient optimization and multithreading. *J Comput Chem*. 2010;31(2):455-461. https://doi.org/10.1002/jcc.21334.
29 Laskowski RA, Swindells MB. LigPlot + : multiple ligand-protein interaction diagrams for drug discovery. *J Chem Inf Model*. 2011;51(10):2778-2786. https://doi.org/10.1021/ci200227u.
30 Gul A, Yang FY, Xie C, et al. Pulmonary fibrosis model of mice induced by different administration methods of bleomycin. *BMC Pulm Med*. 2023;23(1):91. https://doi.org/10.1186/s12890-023-02349-z.
31 Hu SD, He WL, Wu GY. Hydroxyproline in animal metabolism, nutrition, and cell signaling. *Amino Acids*. 2022;54(4):513-528. https://doi.org/10.1007/s00726-021-03056-x.
32 Mora AL, Rojas M, Pardo A, et al. Emerging therapies for idiopathic pulmonary fibrosis, a progressive age-related disease. *Nat Rev Drug Discov*. 2017;16(11):755-772. https://doi.org/10.1038/nrd.2017.170.
33 Leung J, Cho Y, Lockey RF, et al. The role of aging in idiopathic pulmonary fibrosis. *Lung*. 2015;193(4):605-610. https://doi.org/10.1007/s00408-015-9729-3.
34 Zhong C, Lei YqQ, Zhang JY, et al. Prognostic function and immunologic landscape of a predictive model based on five senescence-related genes in IPF bronchoalveolar lavage fluid. *Biomedicines*. 2024;12(6):1246. https://doi.org/10.3390/biomedicines12061246.
35 Arbatskiy M, Balandin D. Universal markers of cellular and replicative senescence. *Probl Gerosci*. 2024;14:121-130. https://doi.org/10.37586/2949-4745-3-2024-121-130.
36 Yan S, Sorrell M, Berman Z. Functional interplay between ATM/ATR-mediated DNA damage response and DNA repair pathways in oxidative stress. *Cell Mol Life Sci*. 2014;71(20):3951-3967. https://doi.org/10.1007/s00018-014-1666-4.
37 Rundle S, Bradbury A, Drew Y, et al. Targeting the ATR-CHK1 axis in cancer therapy. *Cancers (Basel)*. 2017;9(5):41. https://doi.org/10.3390/cancers9050041.
38 Baker JR, Daly L, Hassibi S, et al. Senolytic therapy reduces inflammation in epithelial cells from COPD patients and in smoke-exposure mice. *Front Med (Lausanne)*. 2025;12:1451056. https://doi.org/10.3389/fmed.2025.1451056.
39 Ovadya Y, Krizhanovsky V. Strategies targeting cellular senescence. *J Clin Invest*. 2018;128(4):1247-1254. https://doi.org/10.1172/JCI95149.
40 Lelarge V, Capelle R, Oger F, et al. Senolytics: from pharmacological inhibitors to immunotherapies, a promising future for patients' treatment. *NPJ Aging*. 2024;10(1):12. https://doi.org/10.1038/s41514-024-00138-4.
41 Liu F, Bayliss G, Zhuang SG. Application of nintedanib and other potential anti-fibrotic agents in fibrotic diseases. *Clin Sci (Lond)*. 2019;133(12):1309-1320. https://doi.org/10.1042/CS20190249.